

Source of radio emissions induced by the Galilean moons Io, Europa and Ganymede: *in situ* measurements by Juno

C. K. Louis^{1,2,3}, P. Louarn², B. Collet⁴, N. Clément^{2,5}, S. Al Saati^{2,6},
J. R. Szalay⁷, V. Hue⁸, L. Lamy^{3,4}, S. Kotsiaros⁹, W. S. Kurth¹⁰,
C. M. Jackman¹, Y. Wang^{2,11,12}, M. Blanc^{2,5}, F. Allegrini^{13,14},
J. E. P. Connerney¹⁵, D. Gershman¹⁶

¹School of Cosmic Physics, DIAS Dunsink Observatory, Dublin Institute for Advanced Studies, Dublin 15,
Ireland

²IRAP, Université de Toulouse, CNRS, CNES, UPS, Toulouse, France

³LESIA, Observatoire de Paris, Université PSL, CNRS, Sorbonne Université, Université de Paris,
Meudon, France

⁵Laboratoire d'Astrophysique de Bordeaux, Univ. Bordeaux, CNRS, B18N, Allée Geoffroy Saint-Hilaire,
33615 Pessac, France

^oCPTI, CNRS, Institut Polytechnique de Paris, Route de Saclay, 91128 Palaiseau, France

¹Department of Astrophysical Sciences, Princeton University, Princeton, New Jersey, USA

^oAix-Marseille Université, CNRS, CNES, Institut Origines, LAM, Marseille, France

⁹Technical University of Denmark: Kgs. Lyngby, Denmark

¹⁰Department of Physics and Astronomy, University of Iowa, Iowa City, Iowa, USA

¹¹State Key Laboratory of Space Weather, National Space Science Center, Chinese Academy of Sciences, Beijing, China.

¹²College of Earth and Planetary Sciences, University of Chinese Academy of Sciences, Beijing, China.

¹³Southwest Research Institute, San Antonio, Texas, USA

¹⁴Department of Physics and Astronomy, University of Texas at San Antonio, San Antonio, Texas, USA

¹⁵Space Research Corporation, Annapolis, MD, USA 21403

¹⁶NASA Goddard Space Flight Center, Greenbelt, MD, USA

Key Points:

- All Jupiter–moon radio emissions are shown to be similarly triggered by the CMI.
 - The crossed radio sources are colocated with either MAW, RAW or TEB footprints.
 - The crossed radio sources coincide with downward field-aligned currents and Alfvén perturbations.

Corresponding author: C. K. Louis, corentin.louis@dias.ie

33 **Abstract**

34 At Jupiter, part of the auroral radio emissions are induced by the Galilean moons Io,
 35 Europa and Ganymede. Until now, except for Ganymede, they have been only remotely
 36 detected, using ground-based radio-telescopes or electric antennas aboard spacecraft.
 37 The polar trajectory of the Juno orbiter allows the spacecraft to cross the range of mag-
 38 netic flux tubes which sustain the various Jupiter–satellite interactions, and in turn to
 39 sample *in situ* the associated radio emission regions. In this study, we focus on the de-
 40 tection and the characterization of radio sources associated with Io, Europa and Ganymede.
 41 Using electric wave measurements or radio observations (Juno/Waves), *in situ* electron
 42 measurements (Juno/JADE-E), and magnetic field measurements (Juno/MAG) we demon-
 43 strate that the Cyclotron Maser Instability (CMI) driven by a loss-cone electron distri-
 44 bution function is responsible for the encountered radio sources. We confirmed that ra-
 45 dio emissions are associated with Main (MAW) or Reflected Alfvén Wing (RAW), but
 46 also show that for Europa and Ganymede, induced radio emissions are associated with
 47 Transhemispheric Electron Beam (TEB). For each traversed radio source, we determine
 48 the latitudinal extension, the CMI-resonant electron energy, and the bandwidth of the
 49 emission. We show that the presence of Alfvén perturbations and downward field aligned
 50 currents are necessary for the radio emissions to be amplified.

51 **1 Introduction**

52 One of the main objectives of the Juno mission is to probe Jupiter’s auroral regions
 53 *in situ* (Bagenal et al., 2017) and, in particular, to search for the sources of auroral ra-
 54 dio emission. This is made possible by a suite of instruments capable of acquiring high-
 55 quality plasma and wave measurements, such as Waves (Kurth et al., 2017), JADE-E
 56 (Jovian Auroral Distributions Experiment–Electrons, McComas et al., 2017) and MAG
 57 (Connerney et al., 2017). Imagers on-board Juno are also really useful to compare with
 58 auroral emissions in other wavelengths, such as in ultraviolet with the UVS instrument
 59 (Ultraviolet Spectrograph Gladstone et al., 2017).

60 These instruments provide measurements to study the radio wave amplification pro-
 61 cess, and have already been able to locate the position of the sources (Imai et al., 2017,
 62 2019; Louis et al., 2019a) and to confirm the Cyclotron Maser Instability (CMI) as their
 63 underlying generation mechanism (Louarn et al., 2017, 2018; Louis et al., 2017a, 2020;
 64 Collet et al., 2023, and see below for more details).

65 The Galilean moons Io, Europa and Ganymede are known to induce auroral emis-
 66 sions, at radio (Bigg, 1964; Louis et al., 2017b; Zarka et al., 2017, 2018; Jácome et al.,

67 2022), ultraviolet (UV, Prangé et al., 1996; Clarke, 1998; Clarke et al., 2002) and infrared
 68 (Connerney et al., 1993; Mura et al., 2017, 2018) wavelenghts . The motion of the moons
 69 across Jupiter’s magnetosphere in the plasma torus surrounding them (Szalay et al., 2022)
 70 generates an electric field, inducing electric currents and/or Alfvén waves (Goldreich &
 71 Lynden-Bell, 1969; Neubauer, 1980; Saur, 2004) which both accelerate electrons along
 72 the magnetic field lines in the moons’ flux tubes to kilo-electron-volts (keV) energy. Note
 73 that the case of Callisto is not studied here, even if a tentative detection of the Callisto
 74 UV footprint has been reported (Bhattacharyya et al., 2018), and hints of radio emis-
 75 sions have been observed to this day using Galileo and Voyager data (Menietti et al., 2001;
 76 Higgins, 2007), and not seen by Juno.

77 The Io, Europa, and Ganymede induced UV emissions are known to be produced
 78 by downgoing electrons interacting with the Jovian neutral atmosphere. These signa-
 79 tures are observed at the moons’ magnetic footprint and along their tails, i.e the longi-
 80 tudinal extension of these spots in the downstream direction relative to the plasma flow
 81 encountering the moon (Bonfond et al., 2017a, 2017b). Recent *in situ* studies probed the
 82 magnetic field lines connected to these UV footprints, and found that they are consis-
 83 tent with production by Alfvénic interaction (Szalay et al., 2018, 2020a, 2020b; Allegrini
 84 et al., 2020). On the radio side, the moons’ induced emissions are believed to be produced
 85 by the CMI and have already been simulated and well match the observations (Hess et
 86 al., 2008; Louis et al., 2017a, 2019b). This mechanism is also responsible for the auro-
 87 ral radio emission (independent of the moons) and has been verified *in situ* by Louarn
 88 et al. (2017, involving loss-cone electron distribution functions, or EDF), Louarn et al.
 89 (2018, conics-type EDF) and Collet et al. (2023, shell-type EDF). Recently, Louis et al.
 90 (2020) showed with *in situ* Juno measurements that the radio emission induced by the
 91 Jupiter–Ganymede interaction is indeed produced by the CMI, from a loss cone-type EDF,
 92 i.e., a lack in the up-going electron population, with a characteristic energy of 4–15 keV.

93 Since Jupiter–satellite radio and UV emissions are expected/assumed to be colo-
 94 cated (Hess et al., 2010), the question of the link between these emissions at two differ-
 95 ent wavelengths naturally arises. In the Io case, we know that UV and radio auroral emis-
 96 sions are produced by Alfvénic interactions, and that the main and secondary radio emis-
 97 sions are respectively produced on the magnetic field lines connected to the main Alfvén
 98 wing (MAW) and reflected Alfvén wing (RAW) spots, and highly suspected for the Tran-
 99 shemispheric Electron Beam (TEB) spots (Hess et al., 2010; Lamy et al., 2022). But no
 100 simultaneous *in situ* measurements have yet been analyzed. In the Ganymede case, Louis
 101 et al. (2020) showed, extending the work of Szalay et al. (2020a), that radio emission is
 102 produced above a magnetic flux tube mapping to a UV RAW spot. Hue et al. (2022) showed

that radio emission seems to be produced above the TEB spot. Finally in the Europa case, UV emissions have been observed at the moon's footprint and along the moon's footprint tail (Bonfond et al., 2017a, 2017b; Allegrini et al., 2020; Hue et al., 2023; Rabbia et al., 2023), but no simultaneous observation of UV and radio emissions has yet been analyzed.

This study is a follow-up of the Louis et al. (2020) analysis, focusing on the three known types of Jupiter–satellite radio emissions. In Section 2, we briefly recall the theory of the Cyclotron Maser Instability. In Section 3, we present the observations of Jupiter–Io (J–I), –Europa (J–E) and –Ganymede (J–G) radio emission source crossings and calculate the CMI growth rate (whenever possible) and determine the emission parameters. Finally, in Section 4, we summarize and discuss the results.

2 The Cyclotron Maser Instability

The CMI is known to be responsible for the production of auroral radio emission of Earth, Saturn and Jupiter (Wu & Lee, 1979; Le Queau et al., 1984a, 1984b; Wu, 1985; Pritchett, 1986; Treumann, 2006; Mutel et al., 2010; Lamy et al., 2010; Kurth et al., 2011; Louarn et al., 2017, 2018).

In a tenuous and magnetized enough plasma, i.e., wherever the electron plasma frequency f_{pe} is much lower than the electron cyclotron frequency f_{ce} , and with weakly out-of-equilibrium/non-maxwellian relativistic electrons, the CMI can directly amplify X-mode waves at a frequency close to the electron cyclotron frequency f_{ce} , along the surface of a hollow cone. The CMI is a wave–electron instability for which the resonance condition is reached when the Doppler-shifted angular frequency of the wave in the frame of the electrons ($\omega - k_{||}v_{r||}$) is equal to the relativistic gyration frequency of resonant electrons ($\omega_{ce}\Gamma_r^{-1}$):

$$\omega = \omega_{ce} \sqrt{1 - \frac{v_r^2}{c^2}} + k_{||}v_{r||} \quad , \quad (1)$$

with \mathbf{k} the wave vector and v_r the velocity of the resonant particle, and $\Gamma_r^{-1} = \sqrt{1 - v_r^2/c^2}$ the relativistic Lorentz factor. The \perp and $||$ indices represent the perpendicular and parallel components of the wave vector \mathbf{k} or the velocity v_r with respect to the magnetic field B .

131 In the weakly relativistic case ($v_r \ll c$), the above resonance condition can be rewritten
 132 as the equation for a resonant circle in the $[v_{\perp}, v_{||}]$ velocity space:

$$v_{\perp}^2 + (v_{||} - v_0)^2 = v_r^2 \quad , \quad (2)$$

133 defined by its center:

$$v_0 = \frac{k_{||}c^2}{\omega_{ce}} \quad , \quad (3)$$

134 and its radius

$$v_r = \sqrt{v_0^2 - 2c^2\Delta\omega} \quad , \quad (4)$$

135 with

$$\Delta\omega = (\omega - \omega_{ce})/\omega_{ce} \quad (5)$$

136 the frequency shift between the emission frequency and the cyclotron electron frequency.

137 For the CMI to amplify radio emission, the electron distribution function needs to
 138 present a positive $\partial f / \partial v_{\perp}$ gradient along the resonant circle in the velocity space, and
 139 radio waves will be amplified if positive growth rates are presents.

140 The simplified version of the growth rate expression used by Louarn et al. (2017,
 141 2018); Louis et al. (2020) is well adapted to the amplification of X-mode waves prop-
 142 agating at frequencies close to f_{ce} , for a refraction index $N = 1$ and a moderately en-
 143 ergetic ($E \ll 511$ keV) and low-density ($f_{pe} \ll f_{ce}$) plasma. But this expression con-
 144 tains an approximation at low pitch angle, and therefore applies only to growth rate cal-
 145 culation in the loss cone. Therefore to generalize the calculation of growth rate in the
 146 whole electron distribution function, we use the expression of Collet et al. (2023), de-
 147 rived from the dispersion relation in X mode from Le Queau et al. (1984b) (see Annexe
 148 A of Collet et al., 2023, for the full demonstration of the growth rate expression). They
 149 assumed that the plasma is composed of one cold population at thermodynamic equi-
 150 librium and one non-thermal energetic (or hot) population. In this study, the hot elec-
 151 tron density is the one measured by JADE-E for electrons above 1 keV energy.

$$\gamma = \frac{\left(\frac{\pi}{2}\epsilon_h\right)^2}{1 + \left(\frac{\epsilon_c}{2\Delta\omega}\right)^2} c^2 \int_0^{\pi} d\theta v_r^2 \sin^2(\theta) \frac{\partial f_h}{\partial v_{\perp}}(v_0 + v_r \cos(\theta), v_r \sin(\theta)) \quad (6)$$

152 In this equation $\epsilon_{\alpha} = \omega_{p\alpha}/\omega_{ce}$, where $\omega_{p\alpha}$ is the plasma frequency of the hot ($\alpha =$
 153 h) or cold ($\alpha = c$) electrons. f_h is the normalized electron distribution function of hot
 154 electrons ($\int f dv^3 = 1$). In practice, the factor to normalize the distribution function
 155 is $c^3 10^{-18}/n_e$, where n_e is the electron density (in cm^{-3}).

156 Equation 6 means that the growth rate is obtained by integrating $\partial f_h / \partial v_\perp$ along
 157 a resonant circle in the normalized velocity space $[v_{||}, v_\perp]$, defined by its center v_0 (Equa-
 158 tion 3), its radius v_r (Equation 4) and the angle $\phi \subseteq [0-\pi]$ along this circle.

159 By calculating and maximizing the growth rate, we are able to assess the most CMI-
 160 unstable electron population and characterize the resulting amplified waves, and then
 161 obtain the characteristics of the emission (e.g., the energy of the resonant electrons and
 162 the aperture of the beaming angle).

163 One of the 3 anodes of JADE-E is unfortunately not functional. As a result, due
 164 to Juno's spin and its orientation with respect to the magnetic field lines, it sometimes
 165 happens that certain pitch angles are not sampled. In order to calculate the growth rate
 166 of the wave along the different resonance circles in velocity space, JADE-E needs to sam-
 167 ple sufficient pitch angles. If too much of the EDF measurement is missing (60% along
 168 a resonant circle), we cannot calculate the growth rate and determine the characteris-
 169 tics.

170 However, assuming that Juno is located within the radio source region (if the ra-
 171 dio emission is observed very close to, or even below, f_{ce}), we are still able to obtain some
 172 information about the source size and the characteristics of the emission, by measuring
 173 the emission frequency observed by Juno/Waves data. If the EDF is of shell type, i.e.
 174 if $f \leq f_{ce}$, then the resonant circle is centered on $v_0 = 0$, therefore $k_{||} = 0$ (see Equa-
 175 tion 3), and Equation 1 can then be rewritten as:

$$\omega_{shell} = \omega_{ce} \sqrt{1 - \frac{v_r^2}{c^2}} \quad . \quad (7)$$

176 Thus, from the measurements of the local electron cyclotron frequency ($\omega_{ce} = 2\pi f_{ce}$)
 177 and the emission frequency f_{shell} , and using $E = 0.5 \times m_e v^2$ (with $m_e = 511$ keV/c 2
 178 the electron mass), the electron energy in keV in the shell-driven CMI case can be writ-
 179 ten as:

$$E \simeq 255.5 \times \left(1 - \left(\frac{f_{shell}}{f_{ce}} \right)^2 \right) \quad . \quad (8)$$

180 In the case of a loss-cone (lc) type EDF, i.e. if $f > f_{ce}$, in the weakly relativis-
 181 tic case ($v_r \ll c$) the resonant equation can be rewritten as (for more details see Equa-
 182 tions 2–12 of Louis et al., 2019b):

$$\omega_{lc} \simeq \frac{\omega_{ce}}{\sqrt{1 - \frac{v_r^2}{c^2}}} \quad , \quad (9)$$

and therefore the electron energy in keV in the loss cone–driven CMI case can be written as:

$$E \simeq 255.5 \times \left(1 - \left(\frac{f_{ce}}{f_{lc}} \right)^2 \right) \quad (10)$$

3 Observations and Analysis of Radio Emission Sources Crossings

Due to the large extension of Io's tail (Szalay et al., 2020b) and to Juno's polar orbit, the spacecraft crossed Io's magnetic flux tubes at least twice every orbit (North, then South). However, electron fluxes connected to Io's UV aurora are not observed in appreciable or detectable amounts by Juno/JADE–E every transit of these flux tubes. Therefore, during the first 26 Juno perijoves, 18 cases of electron fluxes connected to Io's magnetic flux tube have been reported using the JADE–E measurements (Szalay et al., 2020b). By studying the data from perijoves (PJ) #27 to #31, we report five more cases of Io's tail flux tube crossing where electron fluxes were measured. In the Europa case, electron fluxes connected to Europa's UV aurora were measured ten times (Allegrini et al., 2020; Rabia et al., 2023). Finally, electron flux connected to Ganymede's UV aurora were measured only two times. The first one during PJ #20 (reported by Szalay et al., 2020a; Louis et al., 2020) and the second one during PJ #30 (studied in details by Hue et al., 2022).

For all moon's flux tube crossings detected by JADE–E, we investigate Waves observations to look for radio emission located below 1 % the local electron cyclotron frequency f_{ce} (determined from the local magnetic field amplitude measured by the MAG instrument). We therefore considered these cases as a potential crossing of a radio source. We then study the EDF obtained from JADE–E. Szalay et al. (2020a, 2020b); Allegrini et al. (2020); Rabia et al. (2023) studied the downward electrons and the production of UV emissions linked to these downward electron currents, as well as the presence of Alfvénic current systems capable of accelerating these electrons. We study here the CMI–unstability of measured EDF, in the continuity of Louis et al. (2020). To go further than Louis et al. (2020), we study instability in the whole EDF, to search not only for loss–cone type instabilities, but also shell type. We also study the upward and downward electrons, as well as the magnetic field perturbation, to determine the presence of field aligned currents (FAC) using Wang et al. (2021); Al Saati et al. (2022) method and Alfvén perturbations capable of accelerating electrons.

Downtail distances with respect to the main spot were recently revised using Juno/UVS data. Over 1,600 spectral images of the Io, Europa, and Ganymede UV footprint were analyzed to provide statistical positions of the main Alfvén wing spots. This allowed Hue et al. (2023) to estimate the distance from Juno to the main spot at the time of the source crossings that will be described in this Section, as well as derived observationally an estimation of the Alfvén travel time for each three moons. Note that the actual position of the main Alfvén wing spots is affected by the background magnetospheric conditions (density of the plasma sheet along the field line connected to the satellite footprint and/or magnetic field strength), and therefore shifts of the main Alfvén wing spots mapped to the equatorial region up to $\pm 2^\circ$ (Io), $\pm 4^\circ$ (Europa) and $\pm 5^\circ$ (Ganymede) are not unusual (See Hue et al., 2023, Figures 4, 5, 7). A negative distance to the main spot therefore translate either (i) a source crossing associated with a transhemispheric electron beam located much upstream of the Alfvén wing spots, or (ii) a change in the plasma condition (e.g., lower plasmashell density and/or higher magnetic field magnitude).

3.1 Jupiter–Io radio emission source crossings

Out of the 23 cases where electron fluxes connected to Io’s tail flux tube were measured, simultaneous radio emissions below $1.01 \times f_{ce}$ were observed in only 4 cases. Figure 1 displays Juno measurements around an Io flux tube encounter, during PJ#5 on 2017–03–27 (2017 March 27th) in the Southern hemisphere (already reported by Louis et al., 2019a). Panel (A) presents the Juno/Waves measurements (in low-resolution mode, Kurth et al., 2017) around the perijove (from ~ -1.5 h before to ~ 2.5 h after). Panel (B) is a 5 min zoom-in of panel (A) using Juno/Waves high-resolution mode. The decreasing solid-black and dashed-black lines in panels (A,B) represent respectively the electron cyclotron frequency f_{ce} and $1.01 \times f_{ce}$. Panels (C)–(E) show the Juno/JADE-E measurements of (C) the electron differential number flux (or intensity), (D) the electron distribution function of upgoing electrons and (E) the partial electron density (where all the energy population < 0.1 keV is not accounted for). Figure 1F displays the FAC calculated based on Al Saati et al. (2022)’s method (see sections 1.3 and 2 of their SI for more details). This method used the residual magnetic field perturbation δB , defined as the difference between the Juno/MAG magnetic field measurements and the magnetic field values obtain from the combination of the Connerney et al. (2018) magnetic field and Connerney et al. (1981) current sheet models. The FAC are then calculated from the residual magnetic field perturbation in the azimuthal direction (δB_ϕ).

Figure 1B displays an emission very close to $1.01 \times f_{ce}$, while we observe an enhancement in the electron energy flux (panel C) at a few keV, a strong intensification

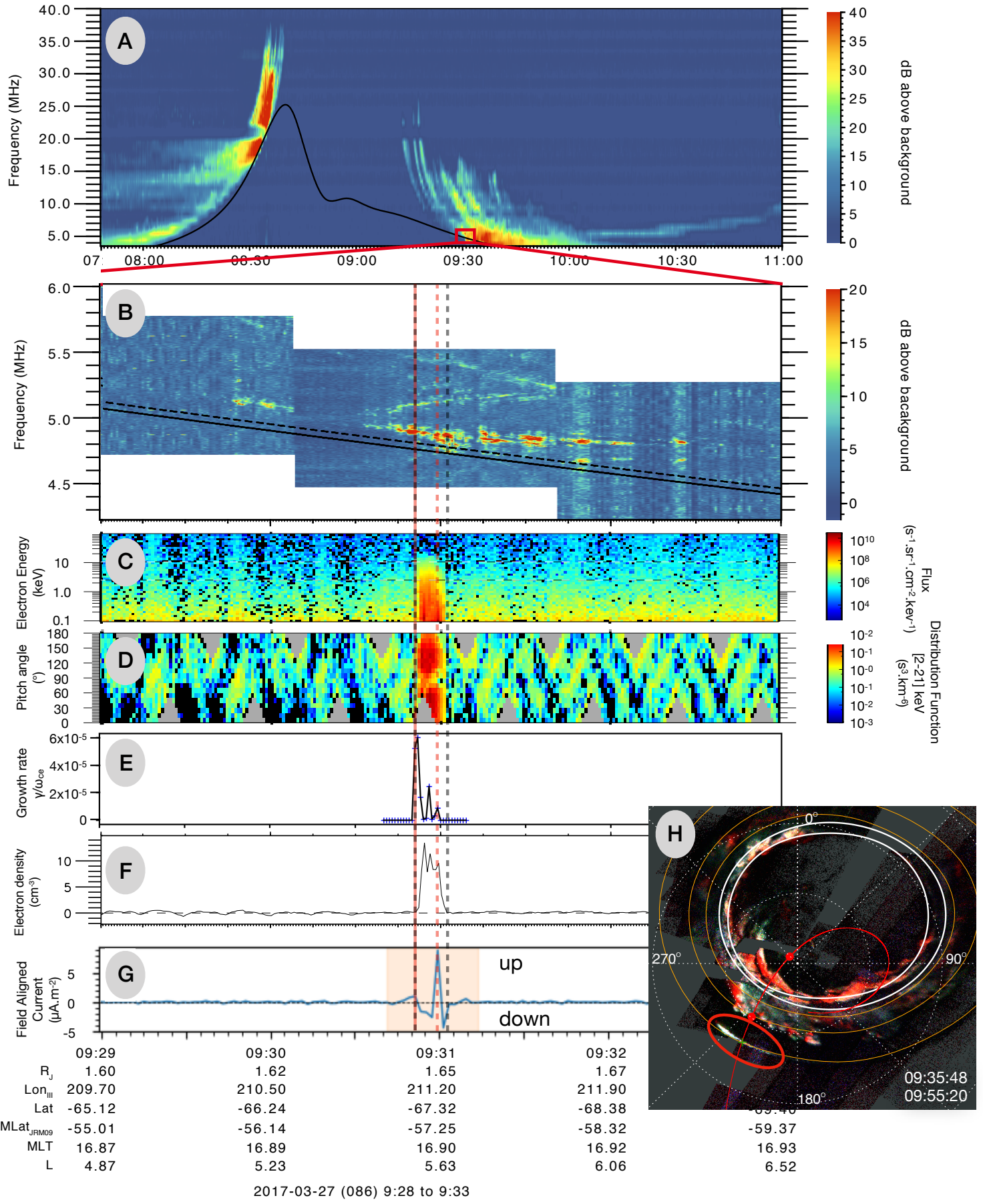


Figure 1: Caption on next page

Figure 1: Juno data during Perijove 5, on 27 March 2017. Panels (A,B) display Juno/Waves data (A) in low-resolution mode and (B) in high-resolution mode. The solid-black lines represent the electron cyclotron frequency derived from the magnetic field measurements of Juno/MAG, and the dashed-black line is $1.01 \times f_{ce}$. Panels (C–D) display Juno/JADE–E measurements: (C) the electron differential number flux (or intensity) of all electrons; (D) the electron distribution function for energy in range [2–21] keV as a function of pitch angles; Panels (E) displays the normalized growth rate γ/ω_{ce} maximal value calculated using Equation 6. Panel (F) shows the partial electron density calculated from the JADE–E flux. Panel (G) shows the field aligned currents calculated based on Al Saati et al. (2022)’s method, using magnetic field fluctuations in the azimuthal direction (δB_ϕ) deduced from the Juno/MAG measurements. The vertical dashed black lines represent the flux tube crossing as inferred from JADE data, while vertical dashed red lines represent the time interval where positive growth rate are calculated from JADE–E measurements. Panel (H) displays a UV map of the southern hemisphere, using Juno/UVS measurements from 09:35:49 to 09:55:20. The red line indicates Juno’s trajectory, with the red dots its position at the start and end time of the measurements used for this image. Io UV footprint is highlighted by the red ellipse.

in the distribution function (panel D), an increase of the electron density (panel F) and a clear upward current surrounded by downward FAC (panel G). Figure S1 in Supporting Information displays the magnetic field fluctuations for all the magnetic field components in spherical coordinates. The magnetic field perturbation associated to the FAC shows clear fluctuations in the transverse component (perpendicular to B, corresponding to δB_ϕ and δB_θ) while no fluctuations are observed in the radial component (δB_r). The fluctuations are therefore confined to the transverse components, which is indicative of a lack of horizontal current, and therefore indicative of FAC (displayed Figure 1F). Moreover, no fluctuations are seen in the total magnetic field magnitude $\delta|B|$, indicating that these variations are Alfvénic in nature (Gershman et al., 2019; Kotsiaros et al., 2019).

Figures 2A–B display the electron distribution function in the velocity space measured by Juno/JADE–E at (A) 09:30:52 and (B) 09:31:00. From these data and Equation 6 we can calculate the normalized growth rate of the emission along different resonant circles to determine the unstable electron population. Figures 2C–D show the estimated normalized growth rate γ/ω_{ce} along resonant circles in the whole EDF, calculated for different centers (x-axis) and different radii (y-axis). Figures 2E–F displays the growth rate γ as a function $\Delta\omega$ for each resonant circle displaying a positive growth rate.

Positive growth rates are obtained for the EDF of Figure 2A, and not for the EDF of Figure 2B. Only resonant circles inside the theoretical loss cone show positive growth rate (blue circles and orange stars in Figure 2E), while no positive growth rate are found for shell-type resonant circles (green diamonds). By doing this calculation before, dur-

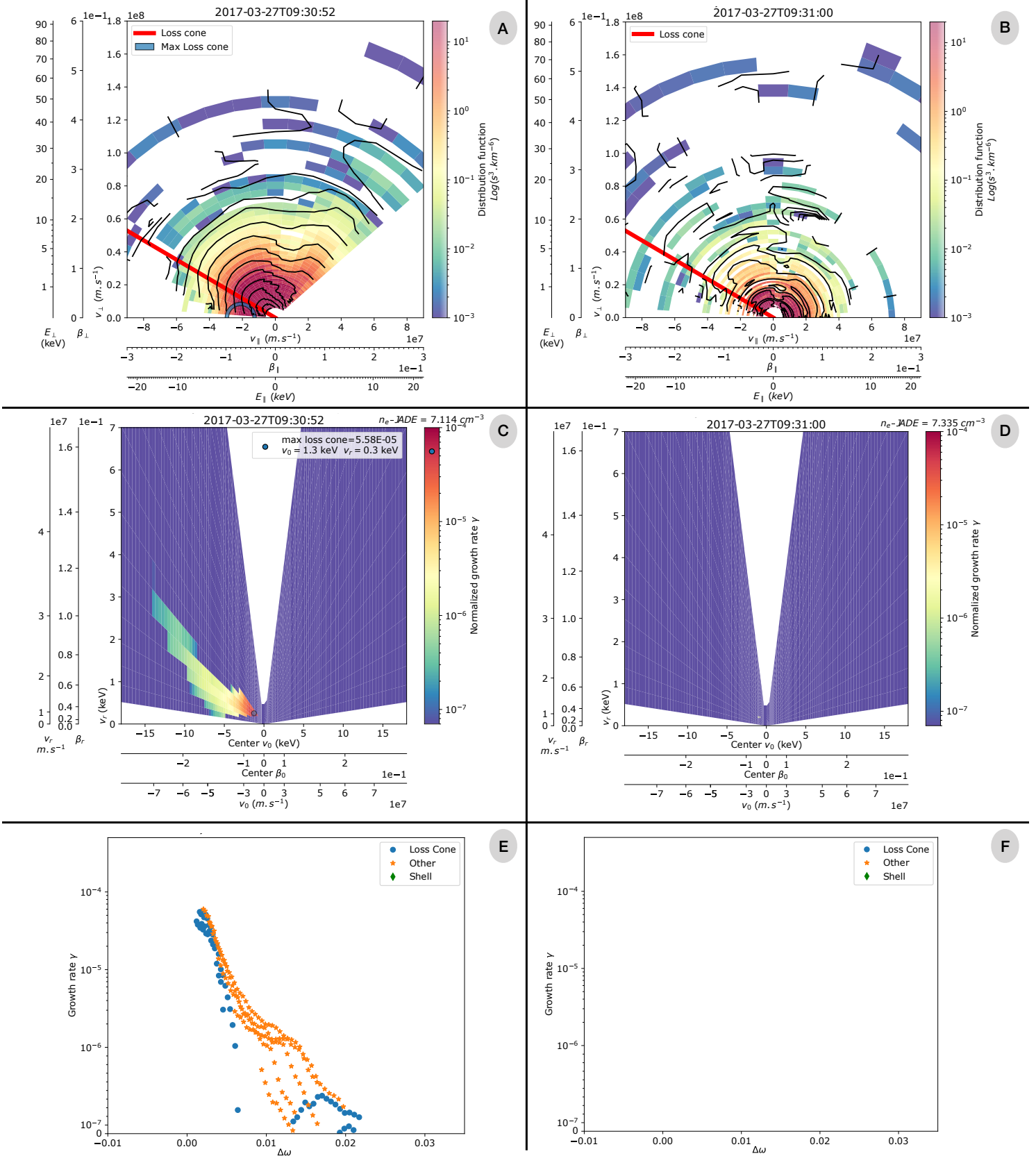


Figure 2: Caption on next page

Figure 2: Panels (A,B): electron distribution function in the velocity space [$v_{||}$, v_{\perp}] measured by JADE-E on 2017–03–27 at (A) 09:30:52 (inside the Io tail radio source) and (B) 09:31:00 (outside the Io tail radio source). In that case, the $v_{||} < 0$ part of the EDF represents upgoing electrons, while $v_{||} > 0$ represents downward electrons. The colorbar and the isocontours are shown using a logarithmic scale in units of $s^3 \cdot km^{-6}$. The radial red thick line indicates the theoretical loss cone value. The blue circular half-circle in panel (A) display the resonant circle with the highest growth rate. Panels (C,D): Normalized growth rate (γ/ω_{ce}) estimates for different resonant circles at different centers v_0 and radii v_r . Panels (E,F): Normalized growth rate as a function of the frequency shift $\Delta\omega$ between the emission frequency and the cyclotron electron frequency (see Equation 11 for all resonant circle with positive growth rate γ). Blue circles represent growth rate for resonant circles tangential to the theoretical value of the loss cone. Orange stars represent growth rate growth rate for resonant circle inside the theoretical loss cone. Both are considered as loss-cone type instabilities. Green diamonds represent growth rate for resonant circles of shell-type.

ing and after the crossing of the Io’s tail flux tube (see Figure 1E), we are able to determine when Juno is in the source, and thus determine its size and the characteristics of the emission. In this case, positive growth rate are obtained along loss-cone type resonant circles from 09:30:51 to 09:30:59 (± 1 sec). This time interval is indicated in Figure 1 by the two vertical dashed red lines. Juno’s velocity being ~ 45 km/s during this time, we determined that the source size is 360 ± 45 km. From the growth rate calculation, we can determine that the energy of the resonant electrons responsible for this emission is in the range [1–15] keV, with an opening angle θ of the beaming cone in the range [74° – 85°]. To determine this value, we used Equation 7 of Louis et al. (2020):

$$\theta = \arccos(\beta_0/(1 + \Delta\omega)) \quad , \quad (11)$$

based on the assumptions of Section 2.

It is interesting to note that enhanced electron fluxes are observed for the period of 09:30:51 to 09:31:02 (determined as the flux tube crossing, Szalay et al., 2020b), while the J-I radio source is only crossed from 09:30:51 to 09:30:59 (determined from the growth rate calculation), which corresponds to the time where Juno is inside a downward current (corresponding to upward electrons). When Juno is located inside an upward current (i.e., downward electrons), no positive growth rate are obtained.

The same method is applied to the data from PJ#6 (North) on 2017–05–19, during which a J-I radio source is crossed between 05:39:31 and 05:39:39 (see Figure S2), and to PJ#29 (North) on 2020–09–16 during which a J-I radio source is crossed between 02:00:34 and 02:00:36 (see Figure S3). For the crossing of the J-I radio source that occurs in the northern hemisphere during PJ#5 on 2017–03–26 around 08:34:40 (see Fig-

ure S4), we do not have JADE–E measurements of the upgoing electrons, and we therefore can not calculate the growth rate. Since no radio emission is observed below f_{ce} , we therefore assume that loss-cone EDF remain the prominent source of free energy for the CMI, and we therefore use Equation 10 to determine the electron energy. The results for these three crossings, i.e., radio source size, resonant electron energy, f_{emission} and opening angle of the beaming cone, are summarized Table 1.

As for PJ#5 (South), FAC and Alfvénic perturbations are observed during PJ#5 (North) and PJ#29 (North) Io's flux tube crossing (see Figures S4 and S3, respectively), with perturbations in the transverse components of the magnetic field (δB_ϕ and δB_θ) while no perturbation is observed in the radial (δB_r) and compressive ($\delta|B|$) components. Furthermore, as for PJ#5 (South), the radio source is not crossed anywhere inside Io's flux tube, but only when Juno is located inside a downward current (i.e., upward electrons). During PJ#6 (North), nothing is observed in the magnetic field perturbations, which could be due to the fact that the electron density is very low ($< 1 \text{ cm}^{-3}$), which could induce a perturbation too weak for the MAG instrument to detect.

Based on the recalculation of the downtail distance to the main spot of Io $\Delta\lambda_{\text{Alfvén}}$ (Hue et al., 2023), the J–I radio emission source crossings of PJ#5 North, PJ#5 South, PJ#6 South are all associated with a Reflected Aflvén Wing (RAW) spot downtail of Io. The intensity of the radio emission seems to be quite similar for crossings occurring close to the main spot, with an intensity of $2\text{--}3 \times 10^{-6} \text{ V}^2 \cdot \text{m}^{-2} \cdot \text{Hz}^{-1}$ when $3.3^\circ < \Delta\lambda_{\text{Alfvén}} < 10.8^\circ$. The intensity seems to be lower when $\Delta\lambda_{\text{Alfvén}}$ is large, with an intensity of $8 \times 10^{-8} \text{ V}^2 \cdot \text{m}^{-2} \cdot \text{Hz}^{-1}$ for $\Delta\lambda_{\text{Alfvén}} = 87.4^\circ$.

3.2 Jupiter–Europa radio emission

During the 26 first perijoves, enhanced electron fluxes connected to Europa's UV aurora were measured ten times (Allegrini et al., 2020; Rabia et al., 2023). A radio source was crossed only during PJ#12 on the Northern hemisphere, on 2018–04–01 around 08:15:44.

Figure 3 displays Juno/Waves (panels A–B), Juno/JADE–E measurements (panels C–E) and Juno/UVS (panel F) during the crossing of flux tube connected to a Europa's downtail UV footprint (Allegrini et al., 2020). During the time of the flux tube crossing, determined by the enhancement of the electron flux in JADE–E measurements (Figures 3C–D), a radio emission is observed below $1.01 \times f_{ce}$ (Figure 3B). However, the JADE–E instruments did not record data of upgoing electrons in the loss cone during this time. We therefore cannot calculate the loss-cone or shell CMI growth rate for this EDF. Since no radio emission is observed below f_{ce} , we therefore assume that loss–

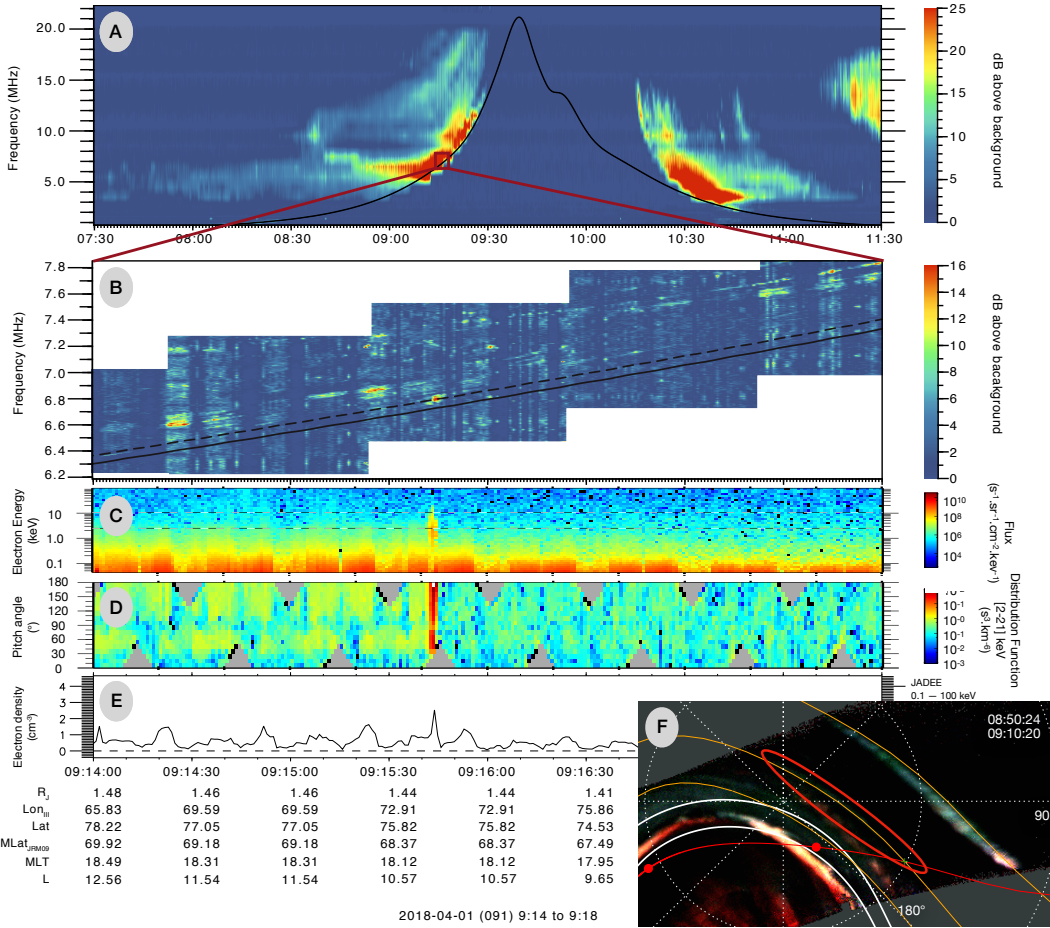


Figure 3: Panels (A,B) display Juno/Waves data (A) in low-resolution mode and (B) in high-resolution mode. The solid-black lines represent the electron cyclotron frequency derived from the magnetic field measurements of Juno/MAG, and the dashed-black line is $1.01 \times f_{ce}$.

Panels (C-E) display Juno/JADE-E measurements: (C) the electron differential number flux (or intensity) of all electrons; (D) the electron distribution function for energy in range [2–21] keV only for pitch angles $[0^\circ–60^\circ]$ corresponding to up-going electrons; (E) partial electron density calculated from the JADE-E flux. Panel (F) displays a UV map of the northern hemisphere, using Juno/UVS measurements from 08:50:24 to 09:10:20. The red line indicates Juno's trajectory, with the red dots its position at the start and end time of the measurements used for this image. Europa UV footprint is highlighted by the red ellipse.

cone EDF remain the prominent source of free energy for the CMI. We then apply Equation 10 to estimate the energy of the resonant electron. Looking at the Juno/Waves measurements (Figure 3B), we determine that the radio emission observed during Europa's flux tube crossing is emitted at a frequency between 0.7 and 1.5% above the electron cyclotron frequency f_{ce} (solid dark line). This frequency measurement leads to an energy of the resonant electrons in the range [3–8] keV, and an opening angle of the beaming cone in the range [79°–84°].

The MAG measurements of the magnetic field perturbation show no strong variation of the different components. Once again, as in the case of PJ#6N for Io, the electron density is very low ($\sim 2 \text{ cm}^{-3}$) which could induce perturbations too weak and/or too short for the MAG instrument to detect.

Based on the latest work of Rabia et al. (2023) and the recalculation of $\Delta\lambda_{\text{Alfvén}}$ (Hue et al., 2023), we can conclude that the J–E radio source crossed during PJ#12 is associated with a Transhemispheric Electron Beam (TEB) spot uptail of the main Europa UV spot.

3.3 Jupiter–Ganymede radio emission

So far, flux tubes connected to Ganymede footprint tail aurora have been crossed twice: the first one during PJ #20 on 2019–05–19 between 07:37:14 and 07:37:32 (reported by Szalay et al., 2020a; Louis et al., 2020) and the second one during PJ #30, on 2020–11–08 around 02:55:02 (Hue et al., 2022).

We already reported the PJ#20N crossing in Louis et al. (2020), but at that time, we did not look at the Juno/MAG measurements, which was done by Szalay et al. (2020a) (and plotted in Figure S5). During this Ganymede footprint tail aurora flux tube crossing, fluctuations in the transverse components (δB_ϕ and δB_θ) were observed, while no fluctuations were measured in the radial (δB_r) and compressive ($\delta|B|$) components, which indicates the presence of field aligned currents and Alfvénic perturbations. As for the J–I radio emission sources, it should be noted that the radio source is only crossed when Juno is in a downward current (i.e., upward electrons). Based on Szalay et al. (2020a); Louis et al. (2020), this radio emissions is associated with a RAW UV spot (with a $\Delta\lambda_{\text{Alfvén}} = 8^\circ$). However, based on the recent work of Hue et al. (2023), for this J–G radio source, $\Delta\lambda_{\text{Alfvén}} = -1.8^\circ$. Therefore, due to the error of 5° on the position of the MAW for Ganymede (due to possible change in the *in situ* plasma condition, see penultimate paragraph of Section 1), it appears that the J–G radio source crossed during PJ#20, is connected not to the RAW spot, but to the MAW spot.

Concerning the second case, during PJ#30 on 2020–11–08 (northern hemisphere), Ganymede footprint tail aurora flux tube was crossed around 02:55:02, with radio emission tangent to $1.01 \times f_{ce}$ at the same time (see Hue et al., 2022). Unfortunately, JADE-E did not measure the upward electrons during Ganymede flux tube crossing. Therefore, we can only estimate the electron energy using Equation 10 (as no radio emission is observed below f_{ce}). Around 02:55:02, Waves measured a radio emission between 1.804 MHz and 1.894 MHz. Based on the Juno/MAG measurements of the magnetic field amplitude, $f_{ce} = 1.7857$ MHz. These values of the emission frequency lead to an estimation of the resonant electron energy in the range [5.1–28.5] keV, and an aperture angle of the beaming cone in the range [70°–81°], provided that Juno actually flew through the radio source. During the crossing, MAG measurements show a ~ 10 nT perturbation in δB_ϕ , while no perturbation is observed in the radial δB_r and compressive $\delta|B|$ components, which indicates again the presence of Alfvénic perturbations and field aligned currents, with an upward current equatorward of a downward current.

Based on the work of Hue et al. (2022), we can also conclude that the J–G radio emission source crossed during PJ#30 is associated with a Transhemispheric Electron Beam (TEB) spot uptail of the main Europa UV spot.

The results for these two J–G radio source crossings are summarized in Table 1.

4 Summary and Discussion

Table 1: Results for the Jupiter–Io, Jupiter–Europa and Jupiter–Ganymede radio emissions source crossings. Is given for each crossing: the name of the moon; the hemisphere of the emission; the associated perijoves; the date and time interval of the radio source crossing as inferred from growth rate calculation when JADE data were available; the JADE data availability; the minimal frequency reached by the radio emission (in MHz); the frequency bandwidth of the emission (in percentage above f_{ce}); the maximum intensity (in $V^2 \cdot m^{-2} \cdot Hz^{-1}$) of the emission; the electron energy (in keV); the opening half-angle of the beaming cone (in °); the radio source size (in km); the downtail distance to the Main Alfvén Wing spot $\Delta\lambda_{Alfvén}$ (Hue et al., 2023); the associated UV emission at the footprint of the magnetic field line associated to the source (MAW: Main Alfvén Wing; RAW: Reflected Alfvén Wing; TEB: Transhemispheric Electron Beam).

Moon Hemisphere Perijove Date (Year–Month–Day) Time interval (HH:MM:SS)	Io South PJ5 2017–03–27 09:30:51–59	Io North PJ5 2017–03–27 around 08:34:40	Io North PJ6 2017–05–19 05:39:31–39	Io North PJ29 2020–09–16 02:00:34–36	Europa North PJ12 2018–04–01 around 09:15:44	Ganymede North PJ20 2019–05–29 07:37:25–30	Ganymede South PJ30 2020–11–08 around 02:55:02
JADE data	Yes	No	Yes	Yes	No	Yes	No
f_{min} (MHz)	4.7	20.8	12.8	27.7	6.7	6.5	1.8
$f_{emission}$ (% > f_{ce})	$3-18 \times 10^{-3}$	$3-29 \times 10^{-3}$	$2-14 \times 10^{-3}$	$5-40 \times 10^{-3}$	$7-15 \times 10^{-3}$	$5-21 \times 10^{-3}$	$5-40 \times 10^{-3}$
Intensity max. ($V^2 \cdot m^{-2} \cdot Hz^{-1}$)	3×10^{-6}	3×10^{-6}	8×10^{-8}	2×10^{-6}	1×10^{-7}	1×10^{-6}	3.5×10^{-9}
Electron energy (keV)	1–15	2–20	1–5	3–10	3–8	4–15	2–20
Opening angle	74–85°	74–85°	77–86°	73–84°	79–84°	76–83°	74–85°
Radio source size (km)	360 ± 45	500 ± 100	415 ± 50	250 ± 50	200 ± 49	250 ± 50	75 ± 50
$\Delta\lambda_{Alfvén}$ (°)	3.3°	10.8°	87.4°	7.8°	–10.5°	–1.8°	–7°
Associated UV emission	RAW	RAW	RAW	RAW	TEB	MAW	TEB

377 Concerning the characteristics of the radio emission, the results are similar for the
 378 three Galilean moons Io, Europa and Ganymede, in terms of driving mechanism (CMI),
 379 electron energy, and beaming. The *in situ* measurements by JADE-E show that the ra-
 380 dio emission is triggered by the Cyclotron Maser Instability, driven by a loss-cone elec-
 381 tron distribution function. No unstable shell-type electron distribution function are de-
 382 tected in JADE-E measurements. The energy of the resonant electrons is in the range
 383 [1–20] keV, and the half-opening cone angle is in the range [74°–86°].

384 These values are in agreement with those recently obtained using ground-based ra-
 385 dio observation, such as the Nançay Decameter Array or NenuFAR, such as the recent
 386 work of Lamy et al. (2022) who determined for Io an opening angle $\theta(f)$ in the range [70°–
 387 80°] and electron energies in the range [3–16] keV. For Europa, Lamy et al. (2023) mea-
 388 sured on an unique detection an opening angle in the range $\theta = [80^\circ\text{--}86^\circ]$ and an elec-
 389 tron energy in the range [0.5–3] keV. For Ganymede, the observations of three emissions
 390 lead them to a determination of a beaming angle in the range $\theta = [71^\circ\text{--}87^\circ]$ and an elec-
 391 tron energy in the range [0.5–15] keV

392 The radio sources have a latitudinal extent of a few hundreds of kilometers. In the
 393 cases where we are able to constrain the radio source location (provided that we have
 394 JADE-E measurement of the up-going electrons), the sources were not crossed anywhere
 395 in the flux tube, but only in the downward Field Aligned Currents.

396 Based on the previous works of Szalay et al. (2020a, 2020b); Louis et al. (2020);
 397 Hue et al. (2022); Rabia et al. (2023) and the recalculated downtail distances from the
 398 UV moon main spot using Hue et al. (2023), we also concluded that in the case of Io,
 399 all radio source crossed were associated with a RAW UV spot. These crossed radio sources
 400 are therefore associated with the secondary radio emissions observed in the usual dynamic
 401 spectrum.

402 In the case of Europa, the only case of radio emission source so far is associated
 403 with a TEB spot. Finally, for Ganymede, one radio source is associated with a MAW
 404 spot, while the second one is associated with a TEB spot. Even if we didn't detect any
 405 radio emission above TEB for Io, these results are in agreement with the interpreta-
 406 tion of the first identification of some Io-DAM linked to the TEB spot analyzed in Lamy
 407 et al. (2022).

408 The maximal intensity is quite similar between all cases close to the main UV spot,
 409 with a value of $2\text{--}3 \times 10^{-6} \text{ V}^2 \cdot \text{m}^{-2} \cdot \text{Hz}^{-1}$ in a interval $3.3^\circ < \Delta\lambda_{\text{Alfvén}} < 10.8^\circ$, with
 410 a decrease of the intensity with long distance downtail ($8 \times 10^{-8} \text{ V}^2 \cdot \text{m}^{-2} \cdot \text{Hz}^{-1}$ for the
 411 case at $\Delta\lambda_{\text{Alfvén}} = 87.4^\circ$). But with only one case very far downtail, we can't produce

412 a fit of this decrease as a function of $\Delta\lambda_{\text{Alfvén}}$. However, the maximal intensity of the
 413 emission is quite smaller for the radio source crossed above a TEB spot ($10^{-9}\text{--}10^{-7} \text{ V}^2.\text{m}^{-2}.\text{Hz}^{-1}$).
 414 This could be related to the type of electron distribution, which seems different near tail
 415 (non-monotonic) than far tail (broadband), at least for Europa with a separation at $\Delta\lambda_{\text{Alfvén}} \simeq$
 416 4° downtail to the Main spot (Rabia et al., 2023).

417 From these latest observations, it therefore appears that the cyclotron maser in-
 418 stability driven by a loss-cone electron distribution function is a common way of ampli-
 419 fying radio emission at Jupiter. This is the case both for auroral radio emission (Louarn
 420 et al., 2017, 2018) and for moon-induced radio emission (Louis et al., 2020; Hue et al.,
 421 2022, and this present study). We have also shown here that the presence of Alfvénic
 422 perturbation as well as field aligned current are necessary for the radio emissions to be
 423 amplified. The radio sources are located only in the downward part of the FAC, i.e. when
 424 the current is carried by upgoing electrons. This supports the results obtained from very
 425 high resolution observations (Zarka et al., 1996; Zarka, 2004; Hess et al., 2007a, 2007b;
 426 Louis et al., 2022), which show that the millisecond bursts observed in the J-I emissions
 427 present only negative drifts, i.e. upward-moving electrons. Finally, radio emission are
 428 found to be associated with TEB, MAW and RAW spot at the footprint of the flux tube
 429 connected to the moons.

430 However, the Cyclotron Maser Instability does not trigger radio emission at a de-
 431 tectable level for Waves every time Juno is in the flux tube of the moons, even if UV emis-
 432 sion is observed at the footprint of the flux tube in each case. Radio sources are crossed
 433 in the two cases of Ganymede flux tube crossings. In contrast, a radio source is crossed
 434 only once over ten Europa flux tube crossings, while for Io, only four radio sources are
 435 crossed over 23 Io flux tube crossings. Therefore, it is clear that several criteria are nec-
 436 essary to amplify a radio wave through the CMI.

437 First, we knew that for the CMI to occur, a low energetic plasma is needed ($f_{pe}/f_{ce} \ll$
 438 0.1). But in this study, we also found that the CMI needs to have a sufficiently dense,
 439 hot and energetic plasma to occur. If the ratio between f_{pe} and f_{ce} is too low, the in-
 440 tegration of the $\delta f/\delta v_\perp$ gradient along the resonant circles gives an insufficiently high
 441 growth rate to amplify the wave to an observable intensity.

442 A second necessary condition seems to be the presence of an Alfvénic acceleration
 443 process and Field Aligned Current. Could the loss-cone-driven CMI be triggered by up-
 444 ward electrons accelerated by a Fermi acceleration process in the FAC generated by the
 445 Alfvén Waves (as suggested by Crary, 1997). To answer this question, more crossings

446 of Jupiter-Moon radio emissions will be necessary, and future Juno observations could
 447 further illuminate these important processes.

448 Data Availability Statement

449 The Juno data used in this manuscript are found at the Planetary Data System
 450 at <https://doi.org/10.17189/1522461> for Waves data (Kurth & Piker, 2022), at <https://doi.org/10.17189/1519715> for JADE-E data (Allegrini et al., 2022) and at <https://doi.org/10.17189/1519711> for MAG data (Connerney, 2017).

453 Acknowledgments

454 The authors thank the Juno mission team, especially the staff of the Waves, JADE and
 455 MAG instruments. C. K. L.'s work at IRAP was supported by CNES. CKL's and CMJ's
 456 work at DIAS was supported by Science Foundation Ireland Grant 18/FRL/6199. C. K.
 457 L. thanks E. Penou, for the help with the particle analysis through the CLWeb software.
 458 V. H. acknowledges support from the French government under the France 2030 invest-
 459 ment plan, as part of the Initiative d'Excellence d'Aix-Marseille Université – A*MIDEX
 460 AMX-22-CPJ-04. The research at the University of Iowa is supported by NASA through
 461 Contract 699041X with the Southwest Research Institute. The research at the South-
 462 west Research Institute is supported by NASA New Frontiers Program for Juno through
 463 contract NNM06AA75C. The french authors acknowledge support from CNES and CNRS/INSU
 464 national programs of planetology (PNP) and heliophysics (PNST).

465 References

- 466 Al Saati, S., Clément, N., Louis, C., Blanc, M., Wang, Y., André, N., ... Mauk,
 467 B. (2022, October). Magnetosphere-Ionosphere-Thermosphere Coupling
 468 Study at Jupiter Based on Juno's First 30 Orbits and Modeling Tools. *Journal*
 469 *of Geophysical Research (Space Physics)*, 127(10), e2022JA030586. doi:
 470 10.1029/2022JA030586
- 471 Allegrini, F., Gladstone, G. R., Hue, V., Clark, G., Szalay, J. R., Kurth, W. S., ...
 472 Wilson, R. J. (2020, September). First Report of Electron Measurements Dur-
 473 ing a Europa Footprint Tail Crossing by Juno. *Geophysical Research Letters*,
 474 47(18), e89732. doi: 10.1029/2020GL089732
- 475 Allegrini, F., Wilson, R. J., Ebert, R. W., & Loeffler, C. (2022). *JJUNO J/SW*
 476 *JOVIAN AURORAL DISTRIBUTION CALIBRATED V1.0, JNO-J/SW-*
 477 *JAD-3-CALIBRATED-V1.0 [dataset]*. doi: 10.17189/1519715
- 478 Bagenal, F., Adriani, A., Allegrini, F., Bolton, S. J., Bonfond, B., Bunce, E. J.,

- 479 ... Zarka, P. (2017, November). Magnetospheric Science Objectives of
 480 the Juno Mission. *Space Science Reviews*, *213*, 219-287. doi: 10.1007/
 481 s11214-014-0036-8
- 482 Bhattacharyya, D., Clarke, J. T., Montgomery, J., Bonfond, B., Gérard, J.-C., &
 483 Grodent, D. (2018, January). Evidence for Auroral Emissions From Cal-
 484 listo's Footprint in HST UV Images. *Journal of Geophysical Research (Space*
 485 *Physics*), *123*, 364-373. doi: 10.1002/2017JA024791
- 486 Bigg, E. K. (1964, September). Influence of the Satellite Io on Jupiter's Decametric
 487 Emission. *Nature*, *203*, 1008-1010. doi: 10.1038/2031008a0
- 488 Bonfond, B., Grodent, D., Badman, S. V., Saur, J., Gérard, J.-C., & Radioti, A.
 489 (2017a, August). Similarity of the Jovian satellite footprints: Spots multiplicity
 490 and dynamics. *Icarus*, *292*, 208-217. doi: 10.1016/j.icarus.2017.01.009
- 491 Bonfond, B., Saur, J., Grodent, D., Badman, S. V., Bisikalo, D., Shematovich, V.,
 492 ... Radioti, A. (2017b, August). The tails of the satellite auroral footprints at
 493 Jupiter. *Journal of Geophysical Research (Space Physics)*, *122*(8), 7985-7996.
 494 doi: 10.1002/2017JA024370
- 495 Clarke, J. T. (1998). Hubble space telescope imaging of jupiter's uv aurora during
 496 the galileo orbiter mission. *Journal of Geophysical Research: Planets*, *103*(E9),
 497 20217-20236. doi: 10.1029/98JE01130
- 498 Clarke, J. T., Ajello, J., Ballester, G., Ben Jaffel, L., Connerney, J., Gérard, J.-C.,
 499 ... Waite, J. H. (2002, February). Ultraviolet emissions from the magnetic
 500 footprints of Io, Ganymede and Europa on Jupiter. *Nature*, *415*, 997-1000.
- 501 Collet, B., Lamy, L., Louis, C. K., Zarka, P., Prangé, R., Louarn, P., ... Kurth,
 502 W. S. (2023). Characterization of Jovian hectometric sources with Juno:
 503 statistical position and generation by shell-type electrons. In C. K. Louis,
 504 Jackman, C. M., G. Fischer, A. H. Sulaiman, & P. Zucca (Eds.), *Planetary,*
 505 *solar and heliospheric radio emissions ix*. Trinity College Dublin, Ireland. doi:
 506 10.25546/103095
- 507 Connerney, J. E. P. (2017). *Juno MAG CALIBRATED DATA J V1.0, JNO-J-3-*
 508 *FGM-CAL-V1.0 [dataset]*. doi: 10.17189/1519711
- 509 Connerney, J. E. P., Acuna, M. H., & Ness, N. F. (1981, September). Modeling
 510 the Jovian current sheet and inner magnetosphere. *Journal of Geophysics Re-*
 511 *search*, *86*, 8370-8384. doi: 10.1029/JA086iA10p08370
- 512 Connerney, J. E. P., Baron, R., Satoh, T., & Owen, T. (1993, November). Images of
 513 Excited H₃⁺ at the Foot of the Io Flux Tube in Jupiter's Atmosphere. *Sci-*
 514 *ence*, *262*, 1035-1038. doi: 10.1126/science.262.5136.1035
- 515 Connerney, J. E. P., Benn, M., Bjarno, J. B., Denver, T., Espley, J., Jorgensen,

- 516 J. L., ... Smith, E. J. (2017, November). The Juno Magnetic Field Investigation.
517 *Space Science Reviews*, 213, 39-138. doi: 10.1007/s11214-017-0334-z
- 518 Connerney, J. E. P., Kotsiaros, S., Oliversen, R. J., Espley, J. R., Joergensen, J. L.,
519 Joergensen, P. S., ... Levin, S. M. (2018, March). A New Model of Jupiter's
520 Magnetic Field From Juno's First Nine Orbits. *Geophysical Research Letters*,
521 45, 2590-2596. doi: 10.1002/2018GL077312
- 522 Crary, F. J. (1997, January). On the generation of an electron beam by Io. *Journal*
523 *of Geophysical Research*, 102(A1), 37-50. doi: 10.1029/96JA02409
- 524 Gershman, D. J., Connerney, J. E. P., Kotsiaros, S., DiBraccio, G. A., Martos,
525 Y. M., -Viñas, A. F., ... Bolton, S. J. (2019, July). Alfvénic Fluctuations
526 Associated With Jupiter's Auroral Emissions. *Geophysical Research Letters*,
527 46(13), 7157-7165. doi: 10.1029/2019GL082951
- 528 Gladstone, G. R., Persyn, S. C., Eterno, J. S., Walther, B. C., Slater, D. C.,
529 Davis, M. W., ... Denis, F. (2017, November). The Ultraviolet Spectrograph
530 on NASA's Juno Mission. *Space Science Reviews*, 213, 447-473. doi:
531 10.1007/s11214-014-0040-z
- 532 Goldreich, P., & Lynden-Bell, D. (1969, April). Io, a jovian unipolar inductor. *Astrophysical Journal*, 156, 59-78. doi: 10.1086/149947
- 533 Hess, S. L. G., Cecconi, B., & Zarka, P. (2008, jul). Modeling of Io-Jupiter decameter
534 arcs, emission beaming and energy source. *Geophysical Research Letters*,
535 35, L13107. doi: 10.1029/2008GL033656
- 537 Hess, S. L. G., Delamere, P., Dols, V., Bonfond, B., & Swift, D. (2010, jun). Power
538 transmission and particle acceleration along the Io flux tube. *Journal of Geophysical Research (Space Physics)*, 115, A06205. doi: 10.1029/2009JA014928
- 540 Hess, S. L. G., Mottez, F., & Zarka, P. (2007b, November). Jovian S burst generation
541 by Alfvén waves. *Journal of Geophysical Research (Space Physics)*,
542 112(A11), A11212. doi: 10.1029/2006JA012191
- 543 Hess, S. L. G., Zarka, P., & Mottez, F. (2007a, January). Io Jupiter interaction, mil-
544 lisecond bursts and field-aligned potentials. *Planetary Space Science*, 55(1-2),
545 89-99. doi: 10.1016/j.pss.2006.05.016
- 546 Higgins, C. A. (2007, May). Satellite control of Jovian 2-6 MHz radio emission using
547 Voyager data. *Journal of Geophysical Research (Space Physics)*, 112, A05213.
548 doi: 10.1029/2006JA012100
- 549 Hue, V., Gladstone, G. R., Louis, C. K., Greathouse, T. K., Bonfond, B., Szalay,
550 J. R., ... Connerney, J. E. P. (2023, May). The Io, Europa, and Ganymede
551 Auroral Footprints at Jupiter in the Ultraviolet: Positions and Equatorial
552 Lead Angles. *Journal of Geophysical Research (Space Physics)*, 128(5),

- 553 e2023JA031363. doi: 10.1029/2023JA031363
- 554 Hue, V., Szalay, J. R., Greathouse, T. K., Bonfond, B., Kotsiaros, S., Louis, C. K.,
 555 ... Mauk, B. H. (2022, April). A Comprehensive Set of Juno In Situ and
 556 Remote Sensing Observations of the Ganymede Auroral Footprint. *Geophysical*
 557 *Research Letters*, *49*(7), e96994. doi: 10.1029/2021GL096994
- 558 Imai, M., Greathouse, T. K., Kurth, W. S., Gladstone, G. R., Louis, C. K., Zarka,
 559 P., ... Connerney, J. E. P. (2019, Jan). Probing Jovian Broadband Kilometeric
 560 Radio Sources Tied to the Ultraviolet Main Auroral Oval With Juno.
 561 *Geophysical Research Letters*, *46*(2), 571-579. doi: 10.1029/2018GL081227
- 562 Imai, M., Kurth, W. S., Hospodarsky, G. B., Bolton, S. J., Connerney, J. E. P., &
 563 Levin, S. M. (2017, July). Direction-finding measurements of Jovian low-
 564 frequency radio components by Juno near Perijove 1. *Geophysical Research*
 565 *Letters*, *44*, 6508-6516. doi: 10.1002/2017GL072850
- 566 Jácome, H. R. P., Marques, M. S., Zarka, P., Echer, E., Lamy, L., & Louis, C. K.
 567 (2022, September). Search for Jovian decametric emission induced by Europa
 568 on the extensive Nançay Decameter Array catalog. *Astronomy & Astrophysics*,
 569 *665*, A67. doi: 10.1051/0004-6361/202244246
- 570 Kotsiaros, S., Connerney, J. E. P., Clark, G., Allegrini, F., Gladstone, G. R., Kurth,
 571 W. S., ... Levin, S. M. (2019, July). Birkeland currents in Jupiter's magnetosphere
 572 observed by the polar-orbiting Juno spacecraft. *Nature Astronomy*, *3*,
 573 904-909. doi: 10.1038/s41550-019-0819-7
- 574 Kurth, W. S., Gurnett, D. A., Menietti, J. D., Mutel, R. L., Kivelson, M. G., Bunce,
 575 E. J., ... Morooka, M. (2011, January). A Close Encounter with a Saturn
 576 Kilometric Radiation Source Region. In H. O. Rucker, W. S. Kurth, P. Louarn,
 577 & G. Fischer (Eds.), *Planetary, solar and heliospheric radio emissions (pre vii)*
 578 (p. 75-85).
- 579 Kurth, W. S., Hospodarsky, G. B., Kirchner, D. L., Mokrzycki, B. T., Averkamp,
 580 T. F., Robison, W. T., ... Zarka, P. (2017, November). The Juno
 581 Waves Investigation. *Space Science Reviews*, *213*, 347-392. doi: 10.1007/
 582 s11214-017-0396-y
- 583 Kurth, W. S., & Piker, C. W. (2022). *JUNO E/J/S/SS WAVES CALIBRATED*
 584 *BURST FULL RESOLUTION V2.0, JNO-E/J/SS-WAV-3-CDR-BSTFULL-*
 585 *V2.0 [dataset]*. doi: 10.17189/1522461
- 586 Lamy, L., Colomban, L., Zarka, P., Prangé, R., Marques, M. S., Louis, C. K., ...
 587 Yerin, S. (2022, April). Determining the Beaming of Io Decametric Emissions:
 588 A Remote Diagnostic to Probe the Io-Jupiter Interaction. *Journal of Geophysical*
 589 *Research (Space Physics)*, *127*(4), e30160. doi: 10.1029/2021JA030160

- 590 Lamy, L., Duchêne, A., Mauduit, E., Zarka, P., Yerin, S., Louis, C., ... Theureau,
 591 G. (2023). Probing Jupiter-satellite interactions from the beaming of their
 592 decametric emissions: the case of Europa and Ganymede. In C. K. Louis,
 593 Jackman, C. M., G. Fischer, A. H. Sulaiman, & P. Zucca (Eds.), *Planetary,*
 594 *solar and heliospheric radio emissions IX*. Trinity Dublin College, Ireland. doi:
 595 10.25546/103097
- 596 Lamy, L., Schippers, P., Zarka, P., Cecconi, B., Arridge, C. S., Dougherty, M. K., ...
 597 Coates, A. J. (2010, June). Properties of Saturn kilometric radiation measured
 598 within its source region. *Geophysical Research Letters*, 37(12), L12104. doi:
 599 10.1029/2010GL043415
- 600 Le Queau, D., Pellat, R., & Roux, A. (1984a, January). Direct generation of the au-
 601 roral kilometric radiation by the maser synchrotron instability: An analytical
 602 approach. *Physics of Fluids*, 27(1), 247-265. doi: 10.1063/1.864520
- 603 Le Queau, D., Pellat, R., & Roux, A. (1984b, May). Direct generation of the auroral
 604 kilometric radiation by the maser synchrotron instability: Physical mechanism
 605 and parametric study. *Journal of Geophysical Research*, 89(A5), 2831-2841.
 606 doi: 10.1029/JA089iA05p02831
- 607 Louarn, P., Allegrini, F., McComas, D. J., Valek, P. W., Kurth, W. S., André, N.,
 608 ... Zink, J. L. (2017, May). Generation of the Jovian hectometric radiation:
 609 First lessons from Juno. *Geophysical Research Letters*, 44, 4439-4446. doi:
 610 10.1002/2017GL072923
- 611 Louarn, P., Allegrini, F., McComas, D. J., Valek, P. W., Kurth, W. S., André, N.,
 612 ... Wilson, R. J. (2018, September). Observation of Electron Conics by Juno:
 613 Implications for Radio Generation and Acceleration Processes. *Geophysical*
 614 *Research Letters*, 45(18), 9408-9416. doi: 10.1029/2018GL078973
- 615 Louis, C. K., Hess, S. L. G., Cecconi, B., Zarka, P., Lamy, L., Aicardi, S., &
 616 Loh, A. (2019b, Jul). ExPRES: an Exoplanetary and Planetary Ra-
 617 dio Emissions Simulator. *Astronomy & Astrophysics*, 627, A30. doi:
 618 10.1051/0004-6361/201935161
- 619 Louis, C. K., Jackman, C. M., Grießmeier, J. M., Wucknitz, O., McKenna, D. J.,
 620 Murphy, P. C., ... Vocks, C. (2022, April). Method to observe Jupiter's ra-
 621 dio emissions at high resolution using multiple LOFAR stations: a first case
 622 study of the Io-decametric emission using the Irish IE613, French FR606, and
 623 German DE604 stations. *RAS Techniques and Instruments*, 1(1), 48-57. doi:
 624 10.1093/rasti/rzac005
- 625 Louis, C. K., Lamy, L., Zarka, P., Cecconi, B., & Hess, S. L. G. (2017b, September).
 626 Detection of Jupiter decametric emissions controlled by Europa and Ganymede

- 627 with Voyager/PRA and Cassini/RPWS. *Journal of Geophysical Research*
628 (*Space Physics*), 122, 9228-9247. doi: 10.1002/2016JA023779
- 629 Louis, C. K., Lamy, L., Zarka, P., Cecconi, B., Imai, M., Kurth, W. S., ... Levin,
630 S. M. (2017a, September). Io-Jupiter decametric arcs observed by Juno/Waves
631 compared to ExPRES simulations. *Geophysical Research Letters*, 44, 9225-
632 9232. doi: 10.1002/2017GL073036
- 633 Louis, C. K., Louarn, P., Allegrini, F., Kurth, W. S., & Szalay, J. R. (2020, Octo-
634 ber). Ganymede-Induced Decametric Radio Emission: In Situ Observations
635 and Measurements by Juno. *Geophysical Research Letters*, 47(20), e90021. doi:
636 10.1029/2020GL090021
- 637 Louis, C. K., Prangé, R., Lamy, L., Zarka, P., Imai, M., Kurth, W. S., & Connerney,
638 J. E. P. (2019a, November). Jovian Auroral Radio Sources Detected In Situ
639 by Juno/Waves: Comparisons With Model Auroral Ovals and Simultaneous
640 HST FUV Images. *Geophysical Research Letters*, 46(21), 11,606-11,614. doi:
641 10.1029/2019GL084799
- 642 McComas, D. J., Alexander, N., Allegrini, F., Bagenal, F., Beebe, C., Clark, G., ...
643 White, D. (2017, November). The Jovian Auroral Distributions Experiment
644 (JADE) on the Juno Mission to Jupiter. *Space Science Reviews*, 213, 547-643.
645 doi: 10.1007/s11214-013-9990-9
- 646 Menietti, J. D., Gurnett, D. A., & Christopher, I. (2001). Control of Jovian radio
647 emission by Callisto. *Geophysical Research Letters*, 28, 3047-3050. doi: 10
648 .1029/2001GL012965
- 649 Mura, A., Adriani, A., Altieri, F., Connerney, J. E. P., Bolton, S. J., Moriconi,
650 M. L., ... Olivieri, A. (2017, June). Infrared observations of Jovian aurora
651 from Juno's first orbits: Main oval and satellite footprints. *Geophysical Re-*
652 *search Letters*, 44(11), 5308-5316. doi: 10.1002/2017GL072954
- 653 Mura, A., Adriani, A., Connerney, J. E. P., Bolton, S., Altieri, F., Bagenal, F.,
654 ... Turrini, D. (2018, August). Juno observations of spot structures and a
655 split tail in Io-induced aurorae on Jupiter. *Science*, 361(6404), 774-777. doi:
656 10.1126/science.aat1450
- 657 Mutel, R. L., Menietti, J. D., Gurnett, D. A., Kurth, W., Schippers, P., Lynch,
658 C., ... Cecconi, B. (2010, October). CMI growth rates for Saturnian
659 kilometric radiation. *Geophysical Research Letters*, 37(19), L19105. doi:
660 10.1029/2010GL044940
- 661 Neubauer, F. M. (1980, March). Nonlinear standing Alfvén wave current system
662 at Io - Theory. *Journal of Geophysics Research*, 85, 1171-1178. doi: 10.1029/
663 JA085iA03p01171

- 664 Prangé, R., Rego, D., Southwood, D., Zarka, P., Miller, S., & Ip, W. (1996, January). Rapid energy dissipation and variability of the lo-Jupiter electrodynamic circuit. *Nature*, *379*, 323-325. doi: 10.1038/379323a0
- 665
- 666
- 667 Pritchett, P. L. (1986, December). Cyclotron maser radiation from a source structure localized perpendicular to the ambient magnetic field. *Journal of Geophysical Research*, *91*(A12), 13569-13582. doi: 10.1029/JA091iA12p13569
- 668
- 669
- 670 Rabia, J., Hue, V., Szalay, J. R., André, N., Nénon, Q., Blanc, M., ... Sulaiman, A. H. (2023). Evidence for non-monotonic and broadband electron distributions in the europa footprint tail revealed by juno in situ measurements. *Geophysical Research Letters*, *50*(12), e2023GL103131. Retrieved from <https://agupubs.onlinelibrary.wiley.com/doi/abs/10.1029/2023GL103131> (e2023GL103131 2023GL103131) doi: <https://doi.org/10.1029/2023GL103131>
- 671
- 672
- 673
- 674
- 675
- 676 Saur, J. (2004, January). A model of Io's local electric field for a combined Alfvénic and unipolar inductor far-field coupling. *Journal of Geophysical Research (Space Physics)*, *109*, A01210. doi: 10.1029/2002JA009354
- 677
- 678
- 679 Szalay, J. R., Allegrini, F., Bagenal, F., Bolton, S. J., Bonfond, B., Clark, G., ... Wilson, R. J. (2020a, February). Alfvénic Acceleration Sustains Ganymede's Footprint Tail Aurora. *Geophysical Research Letters*, *47*(3), e86527. doi: 10.1029/2019GL086527
- 680
- 681
- 682
- 683 Szalay, J. R., Allegrini, F., Bagenal, F., Bolton, S. J., Bonfond, B., Clark, G., ... Wilson, R. J. (2020b, September). A New Framework to Explain Changes in Io's Footprint Tail Electron Fluxes. *Geophysical Research Letters*, *47*(18), e89267. doi: 10.1029/2020GL089267
- 684
- 685
- 686
- 687 Szalay, J. R., Bonfond, B., Allegrini, F., Bagenal, F., Bolton, S., Clark, G., ... Wilson, R. J. (2018, November). In Situ Observations Connected to the Io Footprint Tail Aurora. *Journal of Geophysical Research (Planets)*, *123*(11), 3061-3077. doi: 10.1029/2018JE005752
- 688
- 689
- 690
- 691 Szalay, J. R., Smith, H. T., Zirnstein, E. J., McComas, D. J., Begley, L. J., Bagenal, F., ... Bolton, S. J. (2022, May). Water-Group Pickup Ions From Europa-Genic Neutrals Orbiting Jupiter. *Geophysical Research Letters*, *49*(9), e98111. doi: 10.1029/2022GL098111
- 692
- 693
- 694
- 695 Treumann, R. A. (2006, August). The electron-cyclotron maser for astrophysical application. *Astronomy & Astrophysics*, *453*, 229-315. doi: 10.1007/s00159-006-0001-y
- 696
- 697
- 698 Wang, Y., Blanc, M., Louis, C., Wang, C., André, N., Adriani, A., ... Tao, C. (2021, September). A Preliminary Study of Magnetosphere-Ionosphere-Thermosphere Coupling at Jupiter: Juno Multi-Instrument Measurements
- 699
- 700

- 701 and Modeling Tools. *Journal of Geophysical Research (Space Physics)*, 126(9),
702 e29469. doi: 10.1029/2021JA029469
- 703 Wu, C. S. (1985, August). Kinetic cyclotron and synchrotron maser instabilities
704 - Radio emission processes by direct amplification of radiation. *Space Science
705 Reviews*, 41, 215-298. doi: 10.1007/BF00190653
- 706 Wu, C. S., & Lee, L. C. (1979, June). A theory of the terrestrial kilometric radia-
707 tion. *Astrophysical Journal*, 230, 621-626. doi: 10.1086/157120
- 708 Zarka, P. (2004, December). Fast radio imaging of Jupiter's magnetosphere at low-
709 frequencies with LOFAR. *Planetary Space Science*, 52(15), 1455-1467. doi: 10
710 .1016/j.pss.2004.09.017
- 711 Zarka, P., Farges, T., Ryabov, B. P., Abada-Simon, M., & Denis, L. (1996, January).
712 A scenario for Jovian S-bursts. *Geophysical Research Letters*, 23(2), 125-128.
713 doi: 10.1029/95GL03780
- 714 Zarka, P., Marques, M. S., Louis, C., Ryabov, V. B., Lamy, L., Echer, E., & Cec-
715 coni, B. (2017, January). Radio emission from satellite-Jupiter interactions
716 (especially Ganymede). In G. Fischer, G. Mann, M. Panchenko, & P. Zarka
717 (Eds.), *Planetary radio emissions viii* (p. 45-58). doi: 10.1553/PRE8s45
- 718 Zarka, P., Marques, M. S., Louis, C., Ryabov, V. B., Lamy, L., Echer, E., & Cec-
719 coni, B. (2018, October). Jupiter radio emission induced by Ganymede and
720 consequences for the radio detection of exoplanets. *Astronomy & Astrophysics*,
721 618, A84. doi: 10.1051/0004-6361/201833586

Figure 1.

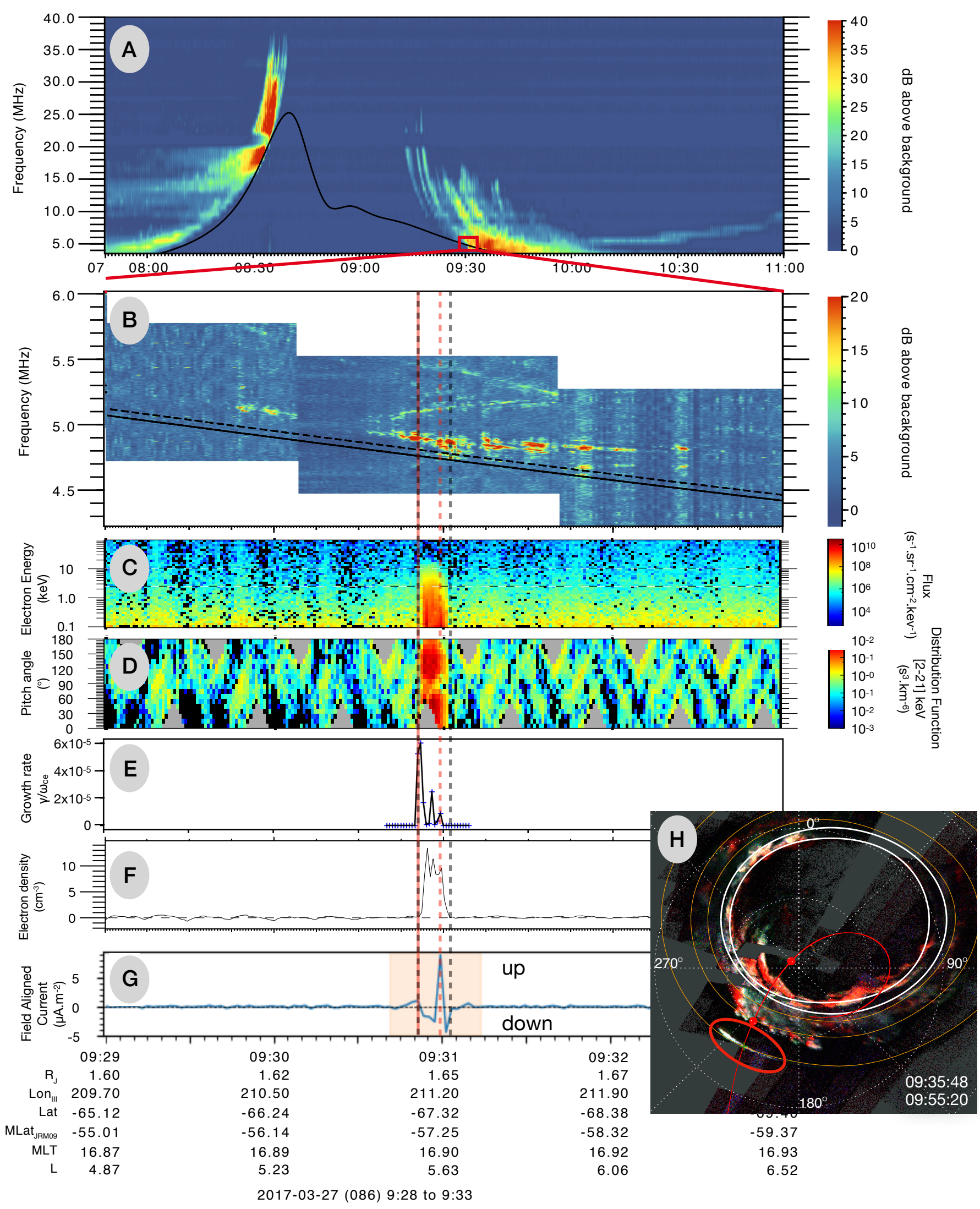


Figure 2.

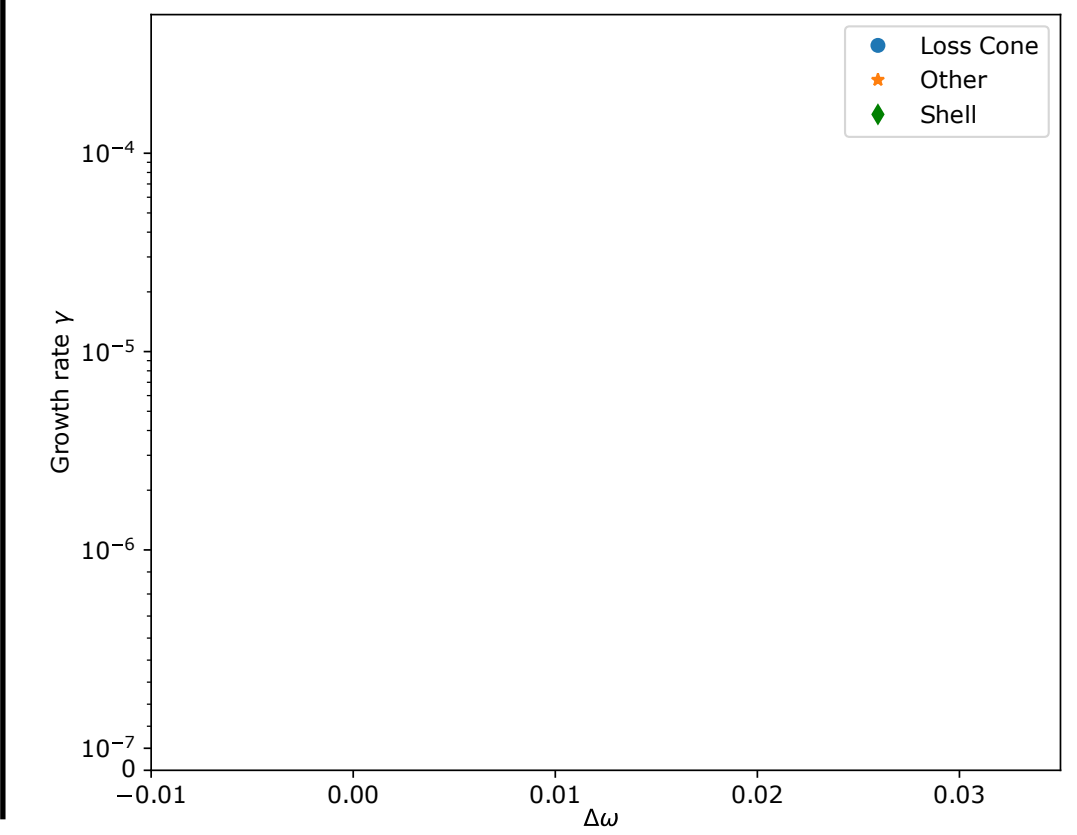
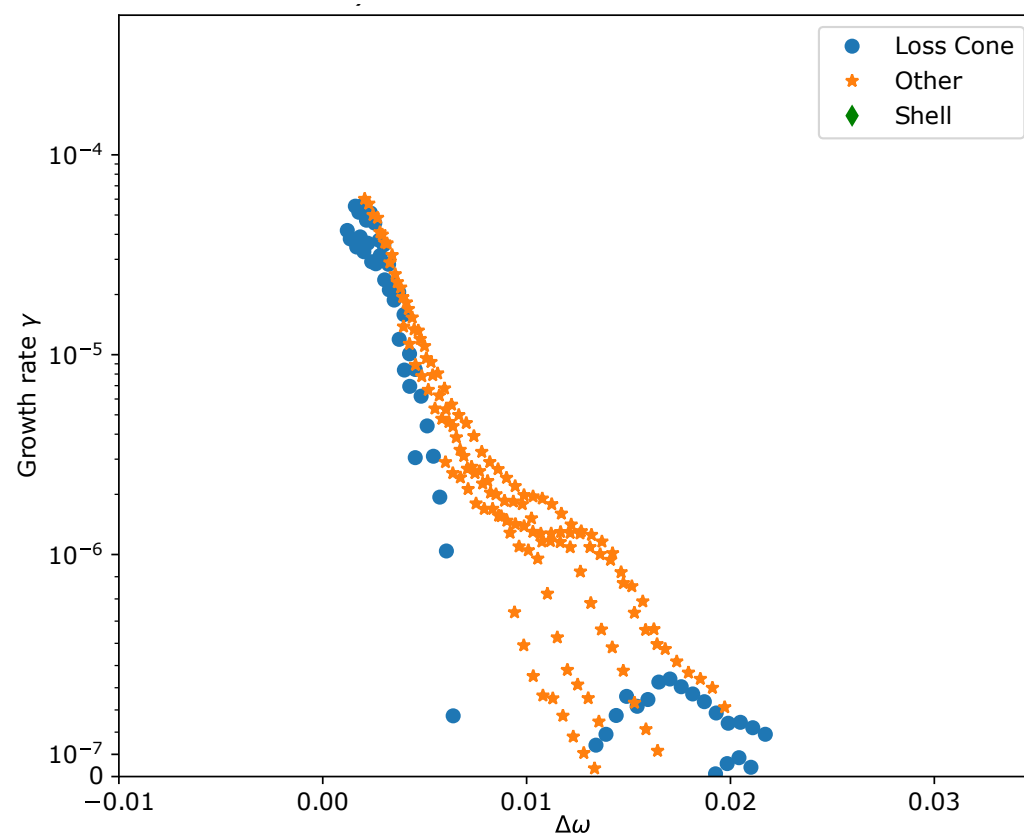
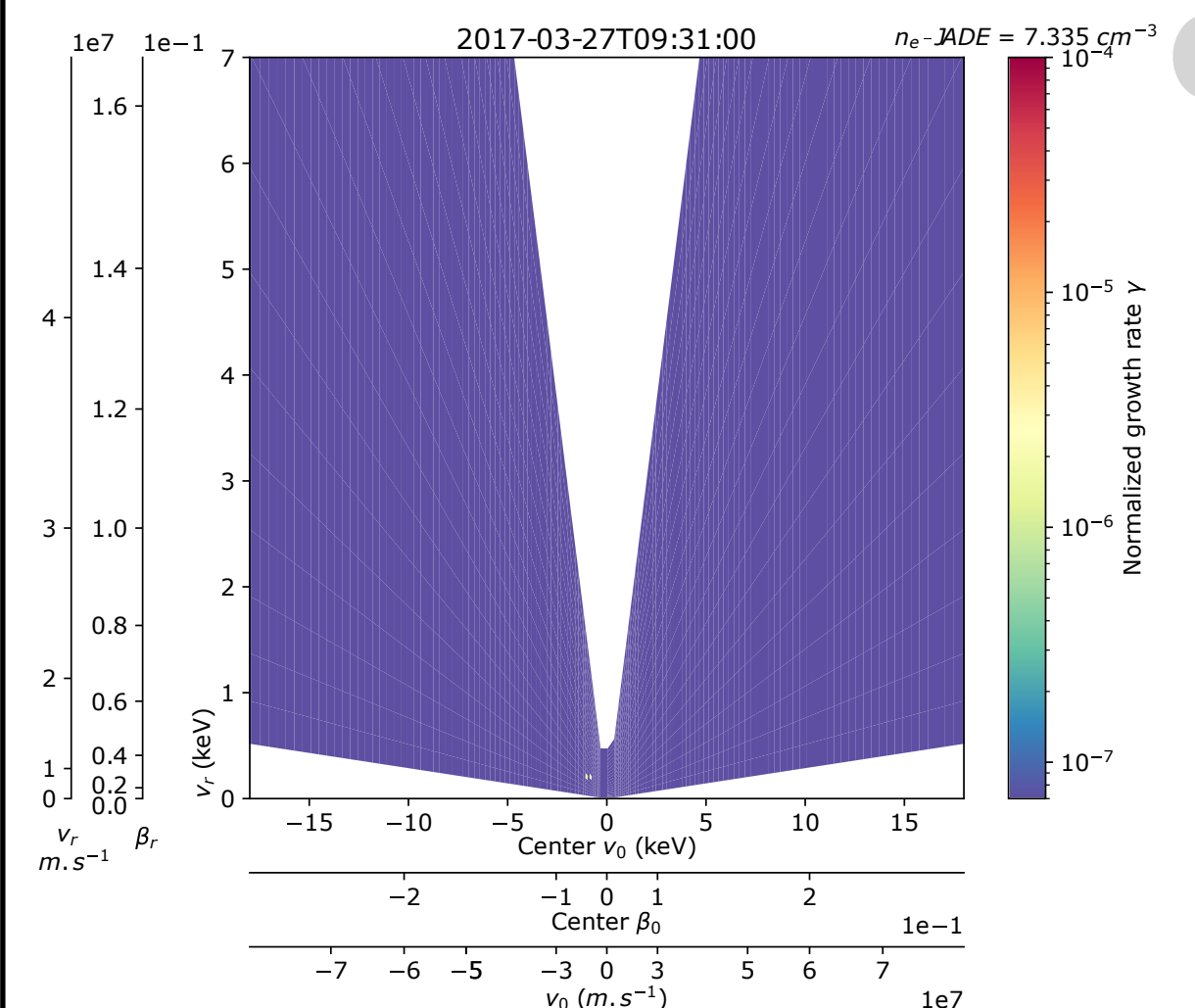
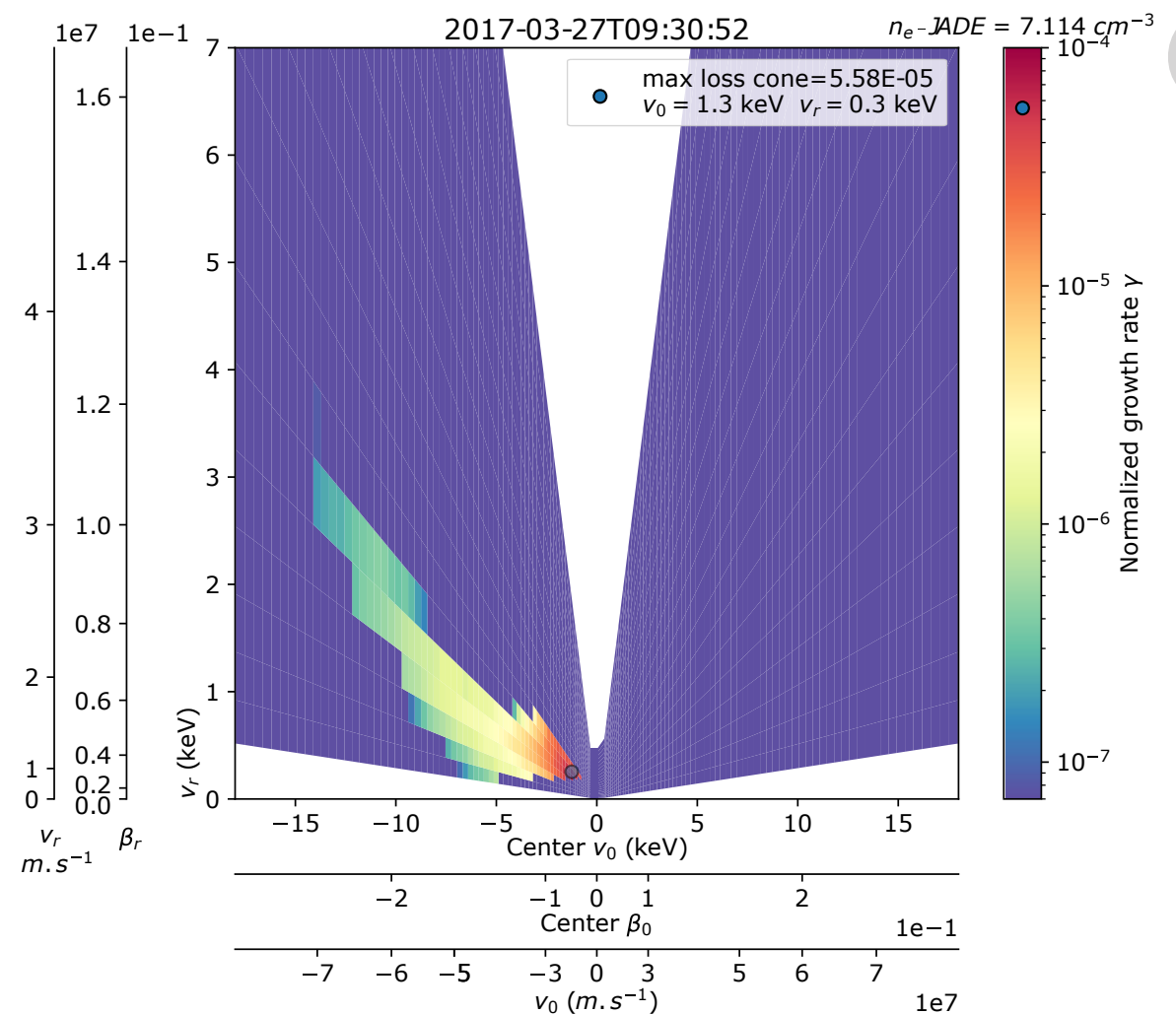
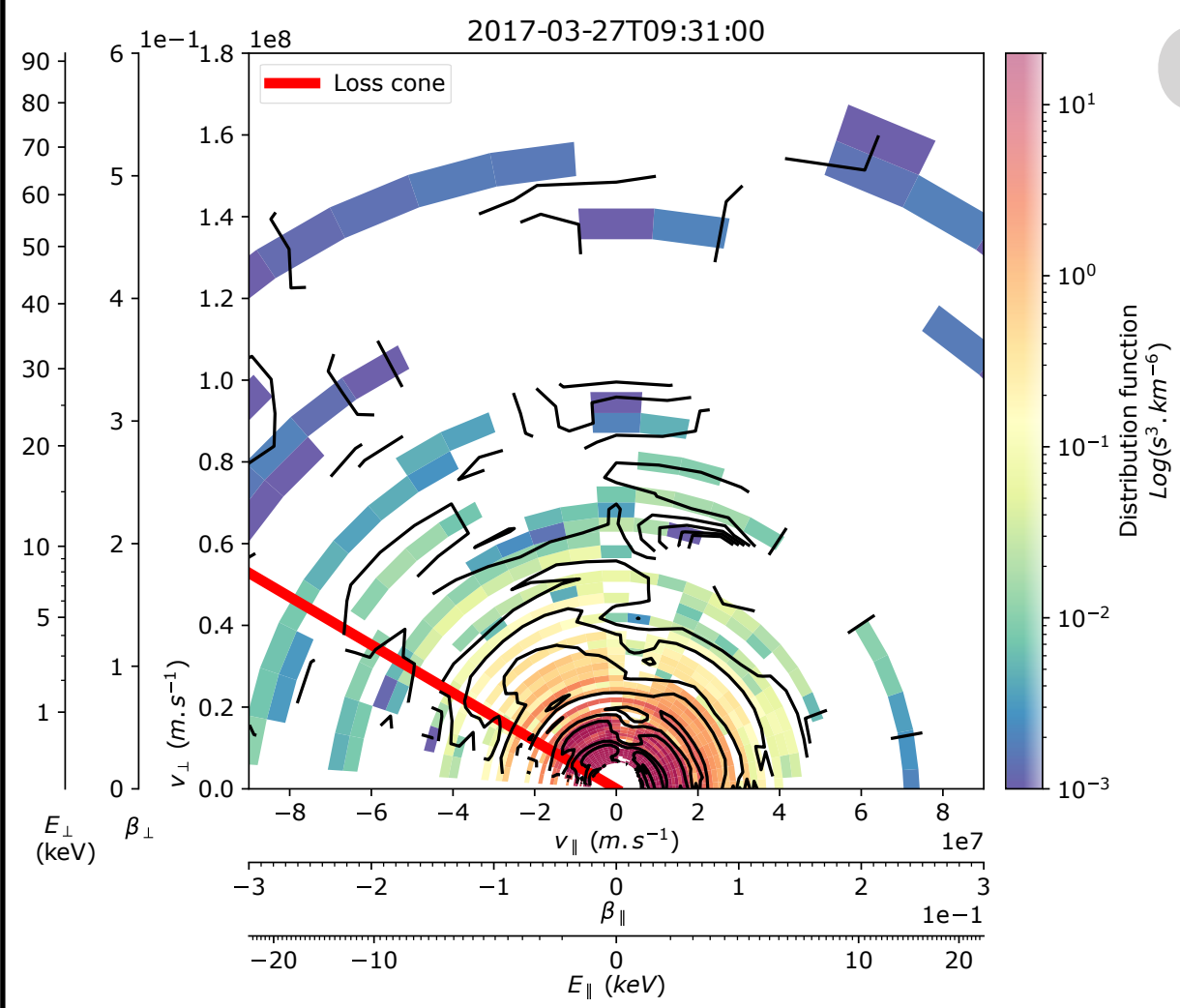
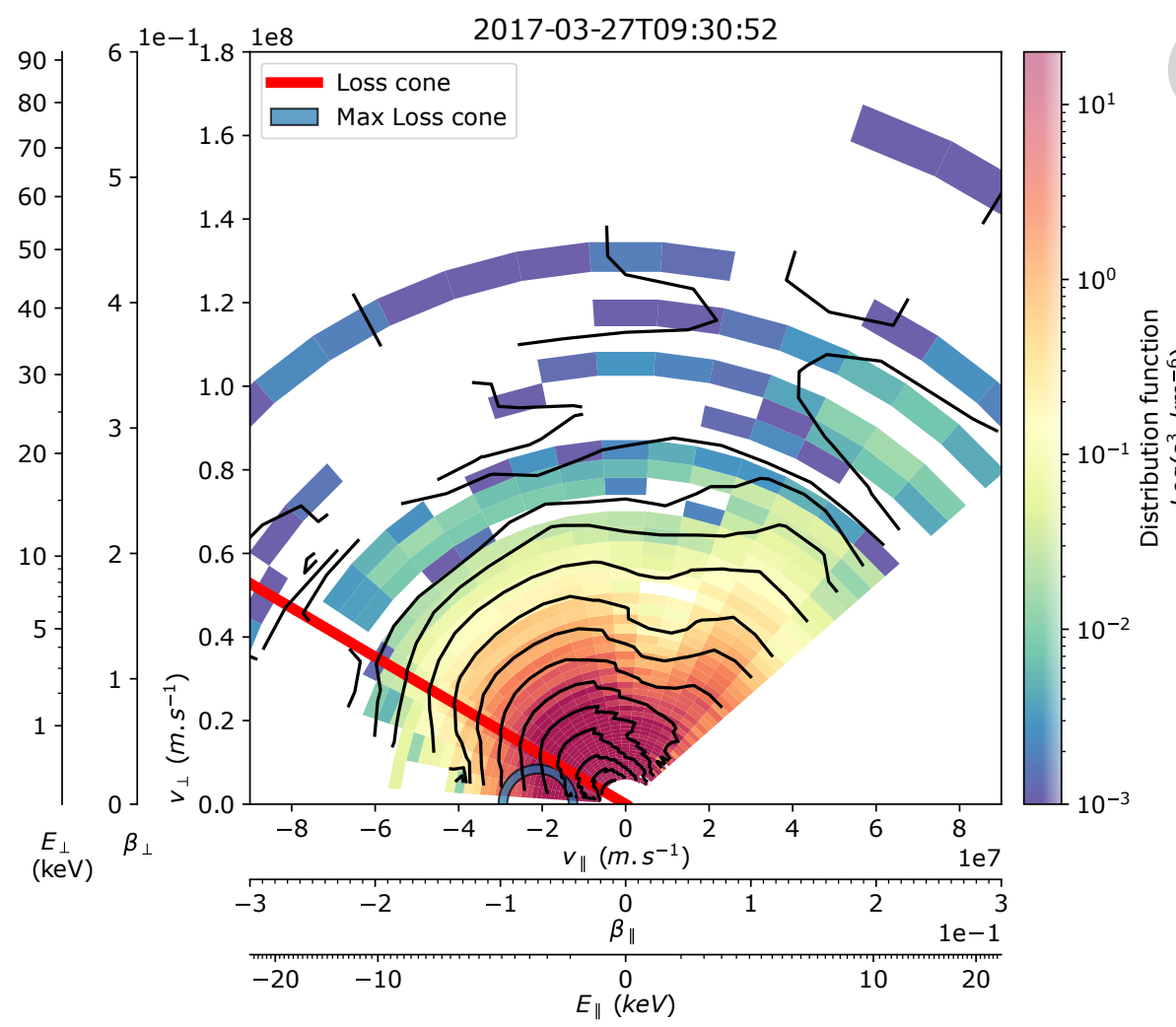


Figure 3.

